Correlation of Processing and Structure in an Ethylene-glycol Side-chain Modified Polythiophene via Combined X-ray Scattering and Four-dimensional Scanning Transmission Electron Microscopy

Andrew A. Herzing, Lucas Q. Flagg, Chad R. Snyder, Lee J. Richter, Jonathan W. Onorato, Christine K. Luscombe, Ruipeng Li*

A. A. Herzing, L. Q. Flagg, C. R. Snyder, L. J. Richter
Material Measurement Laboratory, National Institute of Standards and Technology, Gaithersburg, MD 20899, USA
Email Address: andrew.herzing@nist.gov

J. W. Onorato
Department of Materials Science and Engineering, University of Washington, Seattle, Washington 98195, USA

C. K. Luscombe
pi-Conjugated Polymer Unit, Okinawa Institute of Science and Technology Graduate University, 1919-1 Tanacha, Onna-son, Kunigami-gun, Okinawa, 904-0495, Japan

R. Li
National Synchrotron Light Source II, Brookhaven National Laboratory, Upton, NY 11973, USA

Keywords: *OECT, 4D-STEM, STEM, nanocharacterization*

We report the results of a combined grazing incidence wide-angle X-ray scattering (GIWAXS) and four-dimensional scanning transmission microscopy (4D-STEM) analysis of the effects of thermal processing on poly(3[2-(2-methoxyethoxy)ethoxy]-methylthiophene-2,5-diyl), a conjugated semiconducting polymer used as the active layer in organic electrochemical transistor devices. GIWAXS provides a measure of overall crystallinity in the film, while 4D-STEM produces real-space maps of the morphology and orientation of individual crystallites along with their spatial extent and distribution. The sensitivity of the 4D-STEM detector allows for collection of electron diffraction patterns at each position in an image scan while limiting the imparted electron dose to below the damage threshold. The effects of heat treatment on the distribution and type of crystallites present in the films is determined.

1 Introduction

Conjugated semiconducting polymers are being widely studied for their application in a host of new technologies. For bioelectronic applications, organic electrochemical transistors (OECTs) show great promise due to their unique match to the mechanical properties of tissue and their mixed ionic and electronic conduction [1, 2, 3, 4]. In an OECT, an active polymer layer is patterned with source/drain electrodes on the underside, while the top surface is in contact with an electrolyte solution. When an electrical bias is applied to the solution via a gate electrode, ions from the solution are driven into the polymer in an electrochemical doping process. The result is a change in conductivity of the polymer layer that can be monitored by measuring the current flow between the source and drain. For a p-type accumulation mode device, charge transport is minimal in the undoped state due to the lack of mobile carriers (holes). When the polymer is immersed in the electrolyte solution, the film swells as it absorbs liquid. Upon the application of electrical bias, holes are injected into the film from the bottom electrode and this charge is compensated by the uptake of ions from solution, further swelling the film. Increasing the bias voltage increases the concentration of ions in the film along with the degree of film swelling. Unlike a field-

gated thin-film transistor (TFT), the conductance of the active layer in an OECT is controlled by electrochemical doping of the entire volume of active material. This can involve significant changes in the active layer structure due to the ingress of electrolyte and counter ions. Further structural changes may also occur as a result of the high induced carrier density[5].

Much progress has been made in the development of new, optimized materials for these applications. In particular, the introduction of polar side-chain species to the backbone of OECT polymers has been shown to facilitate the uptake of ions from the aqueous electrolyte at reasonable potentials [6]. In TFTs, it is well established that electrical performance can be extremely sensitive to the detailed microstructure that is a function of both casting conditions and subsequent thermal processing[7, 8, 9, 10]. Strikingly, very little work has been done in studying the role of film processing of the materials being developed for OECTs. It can be anticipated that behavior will be more complex, due to trade-offs between ion uptake and electronic mobility. For example, in one recent study, OECTs with increased crystallinity were shown to exhibit decreased performance [11]. There has been speculation that this behavior can be attributed to the preferential swelling of the amorphous region of the film, however this is difficult to measure experimentally. Moving forward, the ability to spatially resolve the crystalline domains of the polymer is essential to understanding the role of crystallinity and nanoscale morphology on the performance of OECT materials, and therefore enable the design of better OECT materials and processing conditions.

Transmission electron microscopy (TEM) is ideally suited to simultaneously reveal the morphological and structural characteristics of materials organized at nanometer length scales and below. In TEM, a parallel, high-energy electron beam impinges upon a thin specimen and the forward-scattered electrons are collected in various ways to form images of the morphology and structure of the specimen. At low and moderate spatial-resolutions, conventional bright- and dark-field imaging methods can reveal the overall morphology and density variations in organic samples. However, it can be challenging or impossible to use these methods to characterize the crystal structure of organic materials as the high-energy ionizing electron beam rapidly destroys the crystal structure and can even completely vaporize material at elevated dose[12]. To limit specimen damage, low-dose imaging methods can be used to keep the imparted dose below a critical threshold, which is typically in the range of $(1000 - 2000)\ e\ \ = \mathrm{nm}^2$. This approach has been used successfully in the past to map the orientation of crystalline domains in conjugated polymer and small-molecule materials using bright-field lattice imaging [13, 14, 15, 16]. However, the low electron dose can result in noisy images and detection of domains with finer lattice spacing can be challenging.

Alternatively, the TEM can also be operated in scanning (STEM) mode, where the beam is focused to a small spot and scanned over a two-dimensional region of the sample. At each point in the scan, the amount of electron flux collected by one or more post-specimen detectors is stored and this process is repeated serially to form an image. STEM has many advantages over conventional TEM, including the ability to use multiple detectors simultaneously and to precisely control the size of the dose-affected area. One particularly powerful technique available in STEM is known as scanning nanobeam diffraction or four-dimensional (4D)-STEM. In this technique, a two-dimensional electron scattering pattern is collected at every point in a two-dimensional image scan such that the variations in crystallinity and orientation can be measured at nanometer spatial resolutions. Of particular relevance to the present work, Panova *et al.*[17] recently employed 4D-STEM to map the crystalline orientation in a copolymer blend of semi-crystalline poly(3-hexylthiophene-2,5-diyl) (P3HT) and amorphous polystyrene. More recently, the same group reported results from thin films of poly[2,5-bis(3-tetradecylthiophen-2-yl)thieno[3,2-b]thiophene] (PBTTT) and a small-molecule material [18]. In these studies, previous generation CCD-based cameras were employed which are relatively slow and inefficient so that elevated electron doses had to be employed (tens of thousands of electrons per square nanometer) which cannot be used for many polymeric materials. The development of high-sensitivity, direct electron detectors offer a way of surmounting this barrier, as the required data can be collected with a far lower electron dose [19, 20]. *In situ* measure-

ments have even been achieved by using a modified optical approach to 4D-STEM for analysis of dynamic structural changes in a polymer film during heat treatment[21]. Most recently, 4D-STEM has been used to determine the molecular-chain orientations in extremely beam sensitive polymers such as polyethylene [22].

In this paper we discuss the application of 4D-STEM to the characterization of a state of the art OECT material: poly(3[2-(2-methoxyethoxy) ethoxy]methylthiophene-2,5-diyl) (P3MEEMT)[11, 23, 24]. P3MEEMT (see Fig. 1(a)) contains ethylene glycol-based side chains for enhanced ion uptake and exhibits carrier mobilities comparable to state-of-the-art OECT's. We will demonstrate the utility of 4D-STEM for tracking the structural changes with heat treatment in this material. This study is carried out in conjunction with grazing incidence wide-angle X-ray scattering (GIWAXS) measurements. The combination of 4D-STEM and GIWAXS is particularly powerful for probing semi-crystalline polymers such as P3MEEMT. GIWAXS offers sensitivity to nearly all the crystalline features in a film regardless of their orientation. However, the spatial resolution of GIWAXS is very limited and can only provide structural information related to the overall film rather than specific nanoscale features. On the other hand, depending on the experimental setup, 4D-STEM has nano- and sub-nanoscale spatial resolution but typically is only sensitive to in- and out-of-plane structural features. Further, care must be taken when performing a 4D-STEM experiment, as the electron beam can rapidly alter the atomic arrangement in the specimen.

2 Results and discussion

2.1 GIWAXS

GIWAXS measurements were performed in order to assess the crystallinity in the P3MEEMT films and the evolution of the film morphology and structure with thermal annealing. The patterns obtained from as cast and annealed films are presented in Figures 2(a-e). The evident lamellar crystal structure is similar to those observed from other, more widely studied thiophene derivatives such as P3HT; however, the rich evolution with annealing temperature is distinctive. In these patterns, out of plane scattering is indicated along the y-axis while the in-plane scattering occurs along the x-axis. The 100 diffraction peak from the inter-lamellar repeat occurs at q 3.3 nm^{-1} and the 010 diffraction peak from the stacking occurs at approximately 17.0 nm^{-1}. These values correspond to a lamellar repeat distance of 1.9 nm and a stacking distance of 0.4 nm. The former value is somewhat larger than reported for P3HT owing to the longer side chain species present in P3MEEMT [11].

The GIWAXS data show that the as-cast film exhibits little order as the pattern contains only broad, diffuse features. A strong 100 peak is observed upon annealing at 75 °C with pronounced intensity peaks in both the in-plane and out-of-plane orientations. The (200) and (300) peaks can also be seen in the in-plane orientation, indicating a high degree of order within the crystallites. The 100 peak reaches the maximum observed intensity at annealing temperatures of 115 °C and 145 °C before returning to the disordered state at 175 °C. This is consistent with a polymer annealed in the melt and then quickly cooled resulting in a disordered state (Fast scanning Calorimetry (FSC) data reveal an upper melting/clearing temperature of 159 °C (Fig. S2)). The 010 peak intensity is more difficult to track quantitatively since it is positioned at a point in reciprocal space where it overlaps the broad amorphous scattering from the side chains and the background due to the underlying support in a complex manner. However, it can be qualitatively seen that the 010 intensity increases in both the in-plane and out-of-plane orientations with annealing temperature up to 145 °C before decreasing back to a similar value as was observed in the as-cast film. Crystal quality also evolved significantly with temperature (see Table S2). The coherence length of the (100) and (010) crystals was found to increase with annealing temperature up to 145 °C and then dramatically decrease upon heating to 175 °C. Paracrystallinity of the (100) crystals was

also found to decrease from 75 °C to 145 °C, while it could not be estimated for the as cast film and after annealing at 175 °C as there were an insufficient number of orders present.

For the purposes of comparing this data to our subsequent 4DSTEM analysis, only the in-plane scattering, nearest the horizon, is relevant, while in GIWAXS, nearly the entire pole-figure (the beam-specimen orientation) is captured in the 2D pattern. Angular sampling is limited in 4D-STEM, especially for soft organic materials where only a single scan is feasible before structural alteration has occurred. Consequently, 4D-STEM will only be sensitive to those crystallites which are oriented at the Bragg angle with respect to the electron beam. When the beam is parallel to the surface normal of the film, as it is in all cases presented in this paper, the primary reflections arise from the in-plane crystal repeat orientations. In-plane crystallites in P3MEEMT thin films can be present in either a face-on or edge-on orientation. In face-on oriented crystallites, the (100) inter-lamellar repeat is parallel to the substrate surface (*i.e.* in-plane) while the repeat is parallel to the substrate surface normal (*i.e.* out-of-plane). For edge-on oriented crystallites, the orientation of the two crystal repeats is reversed with respect to the substrate. These two crystal orientations are shown schematically in Figures 1(b) and (c), respectively. Appropriate in-plane line-cuts of the GIWAXS patterns are shown in Figure 2f.

2.2 Diffraction Features in 4D-STEM

Turning to the 4D-STEM data, we first focus on data from a film annealed at 115 °C, a temperature at which in-plane crystallinity has been maximized. This data can be inspected in a variety of ways. Most simply, the integrated diffraction data from all scan locations is shown in Figure 3. While some clear differences can be seen, such as sharpening of the high q ring at 17 nm^{-1} upon moderate anneals, they are difficult to interpret since the diffracted features are diluted by the contribution from the amorphous phase. When the individual patterns are examined, three primary types of diffraction patterns were found; an example of each is shown in Figure 4. Patterns collected from many specimen locations do not show any strong diffracted intensity. Instead, only a weakly diffuse background decaying continuously from q=0 is observed (Fig. 4a). The material at these locations is either non-crystalline or is not oriented in the diffraction condition. The background in these experiments is very small since the beam energy (200 keV) is large and the film thickness (50 nm - 80 nm) is small. Outside these amorphous areas, many pixels show strong diffracted intensity at q 3.8 nm^{-1} (Fig. 4b). This is the 100 reflection and indicates the presence of a face-on oriented crystallite at these pixel locations. Often in these pixels, second and third order diffraction peaks are also observed, suggesting that the crystallite quality in these domains is very high and that their orientation is at or very near the Bragg angle. A small minority of pixels where the 100 reflection was observed contained a second set of 100 reflections at a different orientation. This indicates that the beam is sampling two crystallites in the same pixel that are either laterally or vertically adjacent. Finally, a second population of crystallites was observed which showed weaker diffracted intensity at q 18.0 nm^{-1}, corresponding to the (010) stacking in edge-on orientation crystallites (Fig. 4c). These are spatially distinct from the face-on crystallites.

2.3 Virtual Images and Crystallite Orientation

The spatial distribution of crystallites in the film can be directly visualized by extracting virtual images from the 4D-STEM data. This is accomplished by applying an annular mask over the chosen scattering range and integrating the total diffracted intensity. This process is shown graphically in Figure 5(a) where the windows indicate the range of scattering angles which are integrated to produce the virtual images in Figures 5(b) - (d). These 2D real space images provide a map of those regions of the specimen that contribute strongly to the scattered intensity in the associated q range. When this is done for the low q range (blue window in Fig. 5(a)) a virtual bright-field image is produced where bright regions

indicate little to no scattering has occurred and dark regions that scattering has occurred. Virtual images from the 100 and 010 q ranges (green and purple windows in Fig. 5(a), respectively) can be produced in a similar fashion. The resulting virtual image for the 100 diffraction signal reveals a population of crystallites which are elongated in one dimension with an overall length of (40 to 50) nm (Fig. 5(c)). By contrast, the (010) virtual image shows a population of equiaxed crystallites; a morphology which is consistent with the expected out of plane growth habit for this orientation since the projection images produced by 4D-STEM are viewed in parallel to the crystal growth direction.

Since the 4D-STEM data affords us a simultaneous view of the real space crystallite morphology and the reciprocal space structural information, we can unambiguously determine the orientational relationship between the lattice repeat and the crystallite growth direction. Our analysis indicates that the 100 crystallites are elongated in the direction parallel to the crystalline planes giving rise to the diffraction discs. This is demonstrated in Figure 6 which shows several patterns extracted from 100 oriented crystallites in the sample annealed at 115 °C. The diffraction vector in each pattern (*i.e.* the vector from the central, transmitted spot to the diffracted spots) is parallel to the long axis of the corresponding crystallite in the real space image. Note that the orientational relationship between the beam scan/real space images and the detector/diffraction patterns must be properly configured since the beam scan direction can be freely rotated while the detector is fixed (see the Experimental Methods section). The (40 to 50) nm length along the [100] direction of the observed crystallites is consistent with the GIWAXS coherence length of the in-plane population, determined to be (36   10 nm) (Table S2).

By locating the diffraction peaks in all patterns associated with 100 crystallites and determining their relative angle, the orientational distribution of crystallites can be assessed. This is shown in Figure 7 which presents the 100 virtual image (a) alongside a color map (b) showing the growth direction of each crystallite with respect to the vertical axis of the image. The orientation of the face-on crystallites varies continuously indicating no anisotropy was imparted by the blade coating, consistent with negligible optical dichroism in the films. The lower diffracted intensity of the higher-q, edge-on crystallites makes this type of analysis infeasible, but there is no reason to expect an orientation preference of these crystallites when none is observed in their face-on counterpart.

2.4 Effect of Heat Treatment Temperature

4D-STEM datasets were collected using identical conditions from a series of films annealed at 75 °C, 115 °C, 145 °C, and 175 °C. Example diffraction patterns extracted from pixels associated with 100 and 010 crystallites for each heat treatment condition are shown in Figure 8. These patterns were located in the 4D-STEM dataset by locating the most intense pixels in the 100 and 010 virtual images. Patterns from an unannealed, as-cast film (Figure S7) showed no strong diffraction peaks whatsoever. This is expected in P3MEEMT where GIWAXS analysis has indicated that appreciable crystallite formation does not occur until heat treatment has been applied.

Upon heating to 75 °C, some faint traces of 100 diffraction peaks begin to appear, while the 010 peak is not observed. Further heat treatment at 115 °C promotes the increased ordering in the 100 crystallites, where the diffraction peak intensity is much higher than at 75 °C and where second and third order reflections are observed. The 115 °C treatment also promotes the formation of edge-on (in-plane) oriented crystallites whose diffraction peaks are less intense than those associated with face-on oriented crystallites ((100) in-plane). Similar features are observed in the patterns and virtual images from the film annealed at 145 °C as were seen in the 115 °C film. Finally, the patterns extracted from the 175 °C dataset show no strong diffraction features. These patterns and the trends in crystallinity they indicate are also shown as 1D radially integrated plots in Figure 9.

These plots were produced by taking the average of the 50 most intense pixels in the 100 and 010 vir-

tual images and therefore show superior signal above background than the individual patterns shown previously. Because of this, it can be seen that there is a small amount of 100 di racted intensity in the lm annealed at 175 ℃. This temperature is above the P3MEEMT melting point, thus this lm is melt-recrystallized and the minor crystallinity indicates kinetic constraints to re-crystallization during the nominal quench as the lms were free cooled in N_2 upon removal from the hot plate. It should be noted that the fast scanning calorimetry measurements indicate a sensitivity to the exact cooling and heating rates experienced during the anneals, as seen in Fig. S2(c) and (d) and Table S1, which could account for subtle di erences between the GIWAXS and 4D-STEM measurements as the quench conditions are likely faster for the 4D-STEM sample due to the low thermal mass of the silicon nitride TEM membranes. It is just as likely, if not more so, that the small di erences are due to the ability to extract signal from individual crystallites in the 4D-STEM datasets, whereas the signal from the extreme minority is inaccessible in the GIWAXS data. Overall, the crystal-selected 4D-STEM di raction patterns (Figure 9) are in striking agreement with the in-plane GIWAXS patterns (Figure 2f). The real space distribution of the 100 and 010 crystals is shown in the associated virtual images collected in Figure 10.

The trend here matches that already described in the X-ray di raction data. For the 100 images, we can see the formation of poorly ordered crystals at 75 ℃, enhanced crystallinity at 115 ℃ and 145 ℃, and loss of aggregated crystallinity at 175 ℃. In the case of the 010 images, discrete crystals are only observed above 115 ℃. Of particular note is the formation of much smaller crystals upon recrystallization from the melt, as evidenced in both the 4D-STEM (Figure 10) and the coherence length (Table S2). As an interesting aside, based solely on FSC melting temperature, the 1[illegible]5 ℃ anneal uniquely produces the thickest crystallites, likely in the 001 direction (not visible in GIWAXS).

3 Conclusion

The combined GIWAXS and 4D-STEM characterization has revealed a complex, non-monotonic, behavior for P3MEEMT as a function of thermal processing. Crystallinity was found to increase with annealing temperature up to 145 ℃ before decaying back to a disordered state when annealed above the melt (175 ℃). The crystallites that formed upon annealing were observed to be 40 nm to 50 nm in length and the lamellar packing orientation was found to be parallel to the long axis of the crystallites. The orientation distribution of the in-plane crystallites was found to be isotropic. The combination of reciprocal space structural detail and real space visualization of the crystallites could prove to be a valuable tool for diagnosing the role of crystallinity in OECT performance going forward. Further, emerging in-situ cell designs will allow extension of 4D-STEM to characterization of the swollen state, providing critical insight into the role of crystallite separation in charge conduction pathways.

4 Experimental Section

Materials and Sample Preparation

P3MEEMT was synthesized as described previously[11]. Based on size-exclusion, high-performance liquid chromatography, the number average molar mass (Mn) was 23 kg/mol with dispersity, Mw/Mn, of 1.88. Substrates were cleaned by 10 min ultrasonic agitation in each of chloroform and isopropyl alcohol, followed by ultraviolet-ozone treatment for 10 min. P3MEEMT was deposited by blade coating with a custom, low angle coater [25]. The blade height was 200 m and the blade speed nominally 40 mm/s. Substrate temperature was 30 ℃. Blade speed was varied to produce variable lm thickness. The solution was 20 mg/mL in chlorobenzene. Solution was dissolved at 50 ℃ with stirring and allowed to cool to room temperature. Typical lm thickness was 75 nm. Samples were prepared for TEM analy-

sis by rst blade coating a lm of 23 kDa P3MEEMT onto a sacri cial Na:polystyrene sulfonate layer supported on a glass substrate. Next, the lms were delaminated in deionized water and picked up using a silicon nitride TEM membrane. The nitride membrane was necessary to carry out heat treatments at elevated temperature, as the P3MEEMT melt transition occurs at 152 °C and the lms were observed to rupture upon annealing when supported on a traditional copper TEM grid. Heat treatments were performed using a hot plate by placing the grid or membrane directly onto the heated surface for twenty minutes in a nitrogen atmosphere. Samples were made using annealing temperatures of 75 °C, 115 °C, 145 °C, and 175 °C. For GIWAXS, lms were directly deposited on a clean Si wafer.

GIWAXS :
Scattering experiments were performed at the CMS BM-11 beam-line in the NSLS-II at the Brookhaven National Laboratory, NY, USA. GIWAXS patterns were collected with a Pilatus 2D detector by irradiating samples with 13.5 keV X-rays at a nominal 250 mm distance in a vacuum environment. Data were treated and corrected with the NIKA software package[26] within IgorPro environment. GIWAXS patterns were calibrated with a silver behenate sample.

STEM Analysis:
4D-STEM data was collected at room temperature using an FEI Titan 80-300 TEM/STEM operating at 200 keV. A small 5 m probe-forming aperture was used. This aperture is included as part of a custom chip designed by Molecular Foundry [27, 28] and results in a probe convergence semi-angle of 0.3 mrad and a focused probe size of 10 nm FWHM. The small convergence ensures separation of the Bragg di raction discs as well as more strongly peaked di raction features. A Quantum Detectors Merlin direct detection camera with a 256 pixel x 256 pixel array was used to collect the electron scattering patterns using a readout time of 1 msec - 5 msec per pixel with a spatial sampling of 16 nm. Data processing was performed using the FPD Python package [29, 30] along with custom scripts developed for this application[31].

Dose Response Analysis
The dose response of P3MEEMT lms was characterized by collecting a series of 4D-STEM datasets from the same region of the specimen annealed at 115 °C. In order to monitor structural changes with increasing electron dose, a very low probe current was employed for these measurements. The probe current was measured using a calibrated picoammeter attached to the uorescent screen of the microscope. The probe currents employed were quite low (5 pA) making their absolute measurement di cult. However, the measurement is consistent over time making it adequate for determining the instrument parameters for analysis. Patterns collected in this way are shown as a function of electron dose in supplementary Figure S3. Two series are shown, one where the dose per frame was quite low (top row) and another where the dose per frame was increased by holding the probe current constant but increasing the frame acquisition time by a factor of ve. Radial integration of the data from the lower dose series is shown in Figure S4.

A more quantitative analysis of the dose response was then performed by curve tting of the radially averaged di raction patterns. Since the (100) and (010) oriented crystals were not spatially coincident, separate sets of radial pro les were aggregated from the 4D-STEM dose. This was accomplished by generating virtual images from the relevant scattering angles for each di raction feature and identifying the spatial coordinates of the most intense pixels in each case. The patterns at all of these locations were summed to form an integrated di raction pattern for the (100) and (010) oriented crystals and each of these was radially averaged. This process was repeated for each dataset in the series in order to monitor the changes in the (100) and (010) peaks as a function of electron dose. The radially averaged pro les of the low-q and high-q regions are shown in Figure S5. Least-squares curve tting was performed using the Levenberg-Marquardt optimizer as implemented in SciPy. Fits of the (100) and (010) peaks were performed separately over q ranges of (2.0 to 6.5) nm^{-1} and (11.0 to 23.5) nm^{-1}, respectively. In the

(100) case, the model consisted of three functions: a pre-peak exponential, a Gaussian, and a post-peak exponential, while the (010) data was fit with a single pre-peak exponential and a Gaussian. As shown in Figure S6, the position of both peaks follows a linear relationship with electron dose. The (100) peak shifts to higher q while the (010) peak shifts to lower q. A linear fit to both curves shows that the rate of shift in both cases is comparable. These observations indicate that the crystalline unit cell expands in the (010) direction while it contracts in the (100) direction, which is consistent with observations reported elsewhere for polymer bulk heterojunction films[21]. In all subsequent analyses discussed in this paper, the dose was limited to less than 1800 e^{-}/nm^2. This threshold was chosen to limit the intensity decrease in the observed (100) diffraction peaks to 20 %.

Virtual Image Formation and Diffraction Pattern Extraction:
The center of each pattern was determined by a center of mass analysis. To form dark field virtual images, annular reciprocal space masks were created which were centered at $q = (0,0)$ and surrounded the q scattering value for either the 100 or 010 reflections. The masks were applied to each diffraction pattern in the 4D dataset and the remaining intensity was integrated resulting in a 2D array representing the scattered intensity at each scan pixel. Virtual bright field images were formed in a similar fashion except using circular masks centered at $q = (0,0)$. Diffraction patterns associated with each crystallite type were extracted by locating the pixels in the 100 and 010 dark field images which showed the greatest intensity.

Crystallite Orientation Determination:
The orientation of the beam scan with respect to the detector must be properly set so that the reciprocal space scattering directions can be directly related to the real space features. Our detector is oriented at approximately 90° from the slow scan direction of the beam when no scan rotation is applied. To correct this, a 90° rotation is applied to the beam scan and the rotation is finely adjusted by viewing the scan raster on the detector to ensure that the scan proceeds from top to bottom and left to right on the 4D-STEM detector. A crystallite orientation map of the film annealed at 115°C was produced by first masking the data in real space using a binarized version of the 100 virtual image. The threshold for binarization was determined using Otsu's method [32]. Then, the diffraction pattern in each masked pixel was limited to the 100 q range by application of an annular reciprocal space mask centered on the pattern's center of mass. Finally, peak locations were determined using a 2D local maxima detection algorithm on the masked patterns and calculating the inverse tangent of the vector connecting the center of the pattern to the diffraction peak.

Supporting Information

Supporting Information is available from the Wiley Online Library or from the author.

Acknowledgements

Andrew Herzing thanks Meghan Holtz for determining the optimized parameters for the 4D-STEM detector. Work at the Molecular Foundry was supported by the Office of Science, Office of Basic Energy Sciences, of the U.S. Department of Energy under Contract No. DE-AC02-05CH11231. This research used beamline 11-BM (CMS) of the National Synchrotron Light Source, a U.S. Department of Energy (DOE) Office of Science User Facility operated for the DOE Office of Science by Brookhaven National Laboratory under contract no. DE-SC0012704.

References

[1] J. Rivnay, S. Inal, A. Salleo, R. M. Owens, M. Berggren, G. G. Malliaras, Nature Reviews Materials 2018, 3, 2 17086.

[2] G. Malliaras, I. McCulloch, Chemical Reviews 2022, 122, 4 4323.

[3] A. Koklu, D. Ohayon, S. Wustoni, V. Druet, A. Saleh, S. Inal, Chemical Reviews 2022, 122, 4 4581.

[4] C. Pitsalidis, A.-M. Pappa, A. J. Boys, Y. Fu, C.-M. Moysidou, D. van Niekerk, J. Saez, A. Savva, D. Iandolo, R. M. Owens, Chemical Reviews 2022, 122, 4 4700.

[5] G. LeCroy, C. Cendra, T. J. Quill, M. Moser, R. Hallani, J. F. Ponder, K. Stone, S. D. Kang, A. Yu-Lun Liang, Q. Thiburce, I. McCulloch, F. C. Spano, A. Giovannitti, A. Salleo, Materials Horizons 2023, 10 2568.

[6] A. Giovannitti, D.-T. Sbircea, S. Inal, C. B. Nielsen, E. Bandiello, D. A. Hani , M. Sessolo, G. G. Malliaras, I. McCulloch, J. Rivnay, Proceedings of the National Academy of Sciences 2016, 113, 43 12017.

[7] J.-F. Chang, B. Sun, D. W. Breiby, M. M. Nielsen, T. I. Sölling, M. Giles, I. McCulloch, H. Sirringhaus, Chemistry of Materials 2004, 16, 23 4772.

[8] I. McCulloch, M. Heeney, C. Bailey, K. Genevicius, I. MacDonald, M. Shkunov, D. Sparrowe, S. Tierney, R. Wagner, W. Zhang, M. L. Chabinyc, R. J. Kline, M. D. McGehee, M. F. Toney, Nature Materials 2006, 5, 4 328.

[9] A. Salleo, R. J. Kline, D. M. DeLongchamp, M. L. Chabinyc, Advanced Materials 2010, 22, 34 3812.

[10] A. Zen, J. P aum, S. Hirschmann, W. Zhuang, F. Jaiser, U. Asawapirom, J. P. Rabe, U. Scherf, D. Neher, Advanced Functional Materials 2004, 14, 8 757.

[11] L. Q. Flagg, C. G. Bischak, J. W. Onorato, R. B. Rashid, C. K. Luscombe, D. S. Ginger, Journal of the American Chemical Society 2019, 141, 10 4345.

[12] R. F. Egerton, P. Li, M. Malac, Micron 2004, 35, 6 399.

[13] L. F. Drummy, R. J. Davis, D. L. Moore, M. Durstock, R. A. Vaia, J. W. Hsu, Chemistry of Materials 2011, 23, 3 907.

[14] C. J. Takacs, N. D. Treat, S. Krämer, Z. Chen, A. Facchetti, M. L. Chabinyc, A. J. Heeger, Nano Letters 2013, 13, 6 2522.

[15] C. J. Takacs, S. D. Collins, J. A. Love, A. A. Mikhailovsky, D. Wynands, G. C. Bazan, T.-Q. Nguyen, A. J. Heeger, ACS Nano 2014, 8, 8 8141.

[16] C. Cendra, L. Balhorn, W. Zhang, K. O'Hara, K. Bruening, C. J. Tassone, H.-G. Steinrück, M. Liang, M. F. Toney, I. McCulloch, M. L. Chabinyc, A. Salleo, C. J. Takacs, ACS Macro Letters 2021, 10, 10 1306.

[17] O. Panova, X. C. Chen, K. C. Bustillo, C. Ophus, M. P. Bhatt, N. Balsara, A. M. Minor, Micron 2016, 88 30.

[18] O. Panova, C. Ophus, C. J. Takacs, K. C. Bustillo, L. Balhorn, A. Salleo, N. Balsara, A. M. Minor, Nature Materials 2019, 18, 8 860.

[19] C. Ophus, Microscopy and Microanalysis 2019, 25, 3 563.

[20] K. C. Bustillo, S. E. Zeltmann, M. Chen, J. Donohue, J. Ciston, C. Ophus, A. M. Minor, Accounts of Chemical Research 2021, 54, 11 2543.

[21] M. Wu, C. Harrei , C. Ophus, M. Johnson, R. H. Fink, E. Spiecker, Nature Communications 2022, 13, 1 2911.

[22] S. Kanomi, H. Marubayashi, T. Miyata, H. Jinnai, Nature Communications 2023, 14, 1 5531.

[23] B. X. Dong, C. Nowak, J. W. Onorato, J. Strzalka, F. A. Escobedo, C. K. Luscombe, P. F. Nealey, S. N. Patel, Chemistry of Materials 2019, 31, 4 1418.

[24] L. Q. Flagg, C. G. Bischak, R. J. Quezada, J. W. Onorato, C. K. Luscombe, D. S. Ginger, ACS Materials Letters 2020, 2, 3 254.

[25] C. M. Sta ord, K. E. Roskov, T. H. Epps, M. J. Fasolka, Review of Scienti c Instruments 2006, 77, 2 023908.

[26] J. Ilavsky, Journal of Applied Crystallography 2012, 45, 2 324.

[27] S. E. Zeltmann, A. Müller, K. C. Bustillo, B. Savitzky, L. Hughes, A. M. Minor, C. Ophus, Ultramicroscopy 2020, 209 112890.

[28] C. Mahr, K. Müller-Caspary, T. Grieb, F. F. Krause, M. Schowalter, A. Rosenauer, Ultramicroscopy 2021, 221 113196.

[29] M. Nord, R. W. H. Webster, K. A. Paton, S. McVitie, D. McGrouther, I. MacLaren, G. W. Paterson, Microscopy and Microanalysis 2020, 26, 4 653.

[30] G. W. Paterson, R. W. H. Webster, A. Ross, K. A. Paton, T. A. Macgregor, D. McGrouther, I. MacLaren, M. Nord, Microscopy and Microanalysis 2020, 26, 5 944.

[31] A. A. Herzing, MerlinTools, 2021, URL https://github.com/AndrewHerzing/merlintools.

[32] N. Otsu, IEEE Transactions on Systems, Man, and Cybernetics 1979, 9, 1 62.

(c)

(a) (b)

Figure 1: Chemical structure of P3MEEMT (a) along with schematic depictions of the in-plane lamellar repeat distances expected from GIWAXS analysis. Face-on stacking (b, expected in-plane $q = 3.3$ nm^{-1}) and edge-on stacking (c, expected in-plane $q = 17.0$ nm^{-1})

(a) As Cast

(b) 75 ℃

(c) 115 ℃

(d) 145 ℃

(e) 175 ℃

(f)

Figure 2: GIWAXS patterns (a-e) collected from the P3MEEMT thermal annealing series. Also shown is a plot of the intensity along the in-plane direction (x-axis) only (f).

Figure 3: Integrated di racted intensity from all pixels in 4D-STEM datasets collected from P3MEEMT annealed at various temperatures.

(a) (b) (c)

Figure 4: Examples of three classes of di raction patterns observed in 4D-STEM of P3MEEMT lm annealed at 115℃. Pattern (a) is typical of pixels that are amorphous or where the crystal is far from a Bragg orientation. while patterns (b) and (c) are examples of pixels that show 100 (b) or 010 (c) Bragg di raction peaks. All patterns are shown in log scale.

(a)

(b) (c) (d)

Figure 5: Radial average of sum di raction pattern from 4D-STEM data of P3MEEMT annealed at 115 °C (a) along with virtual images (b-d) extracted from three di erent q ranges. The images highlight the bright- eld signal (b), the 100 di raction peaks (c), and 010 di raction peaks (d). For visual purposes, each image is scaled based on the intensity range.

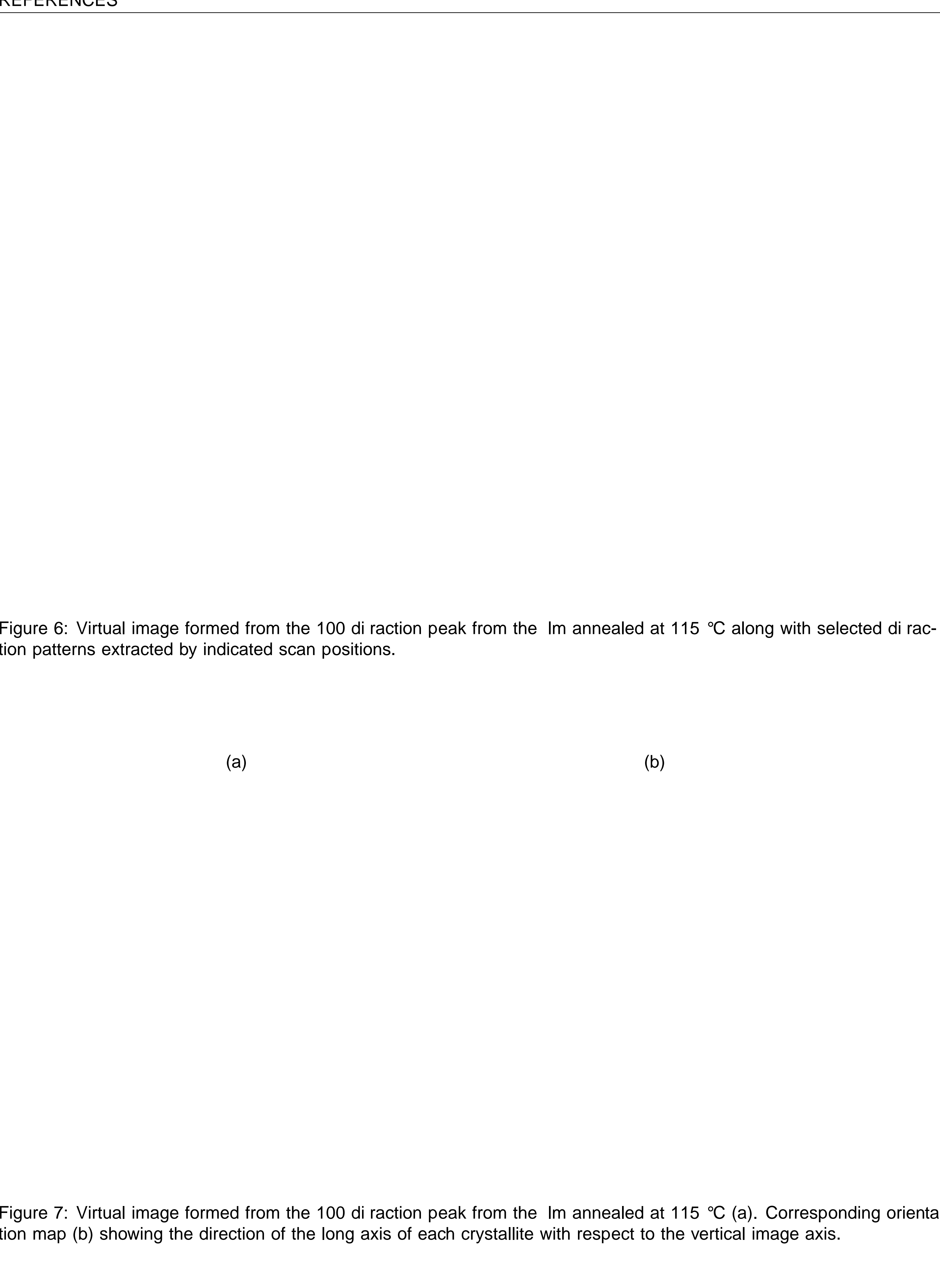

Figure 6: Virtual image formed from the 100 di raction peak from the lm annealed at 115 °C along with selected di raction patterns extracted by indicated scan positions.

(a) (b)

Figure 7: Virtual image formed from the 100 di raction peak from the lm annealed at 115 °C (a). Corresponding orientation map (b) showing the direction of the long axis of each crystallite with respect to the vertical image axis.

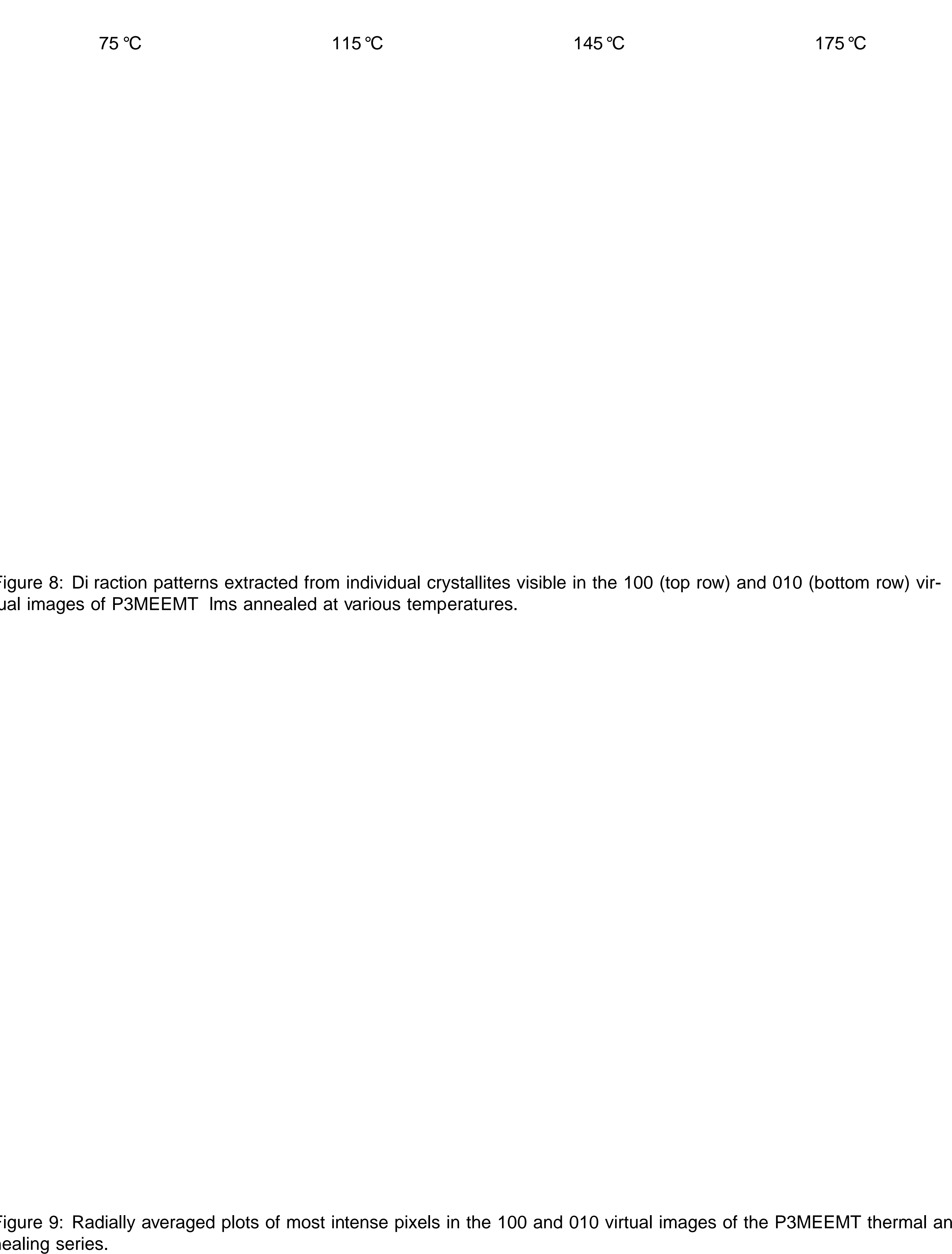

Figure 8: Di raction patterns extracted from individual crystallites visible in the 100 (top row) and 010 (bottom row) virtual images of P3MEEMT lms annealed at various temperatures.

Figure 9: Radially averaged plots of most intense pixels in the 100 and 010 virtual images of the P3MEEMT thermal annealing series.